



## Predicted a honeycomb metallic BiC and a direct semiconducting Bi<sub>2</sub>C monolayer as excellent CO<sub>2</sub> adsorbents

Menghui Xi<sup>a</sup>, Chaozheng He<sup>a,\*</sup>, Houyong Yang<sup>a</sup>, Xi Fu<sup>b,d,\*</sup>, Ling Fu<sup>c,\*</sup>, Xiaoli Cheng<sup>d</sup>, Jiyuan Guo<sup>e</sup>

<sup>a</sup> Institute of Environmental and Energy Catalysis, Shaanxi Key Laboratory of Optoelectronic Functional Materials and Devices, School of Materials Science and Chemical Engineering, Xi'an Technological University, Xi'an 710021, China

<sup>b</sup> College of Science, Hunan University of Science and Engineering, Yongzhou 425199, China

<sup>c</sup> College of Resources and Environmental Engineering, Tianshui Normal University, Tianshui 741001, China

<sup>d</sup> Department of Physics, Jishou University, Jishou 416000, China

<sup>e</sup> School of Science, Jiangsu University of Science and Technology, Zhenjiang 212003, China

### ARTICLE INFO

#### Article history:

Received 3 December 2021

Revised 13 December 2021

Accepted 15 December 2021

Available online 20 December 2021

#### Keywords:

First-principles calculation

Global optimization method

Monolayer

Bismuth carbide compounds

CO<sub>2</sub> adsorbents

Semiconducting

### ABSTRACT

We predicted two stable two-dimensional materials of carbon and bismuth elements, namely BiC and Bi<sub>2</sub>C monolayers. The stabilities of two monolayers were examined by cohesive energy, Born criteria, first-principle MD simulations and phonon spectra, respectively. By including the spin-orbit coupling effects, the BiC monolayer is a metal and the Bi<sub>2</sub>C monolayer possesses a narrow direct (indirect) band gap of 0.403 (0.126) eV under the HSE06 (GGA-PBE) functional. For the adsorption of CO<sub>2</sub> molecules, the BiC and Bi<sub>2</sub>C monolayers have three stable adsorption sites C2, T3 and T4 with the adsorption energies as -0.57, -0.51 and -0.81 eV, and the activation ability on the adsorption as T4 > T3 > C2. These consequences make the BiC and Bi<sub>2</sub>C monolayers to be promising adsorbents to capture CO<sub>2</sub> gas, the Bi<sub>2</sub>C monolayer to be well photovoltaics and optoelectronics material, and the BiC monolayer to be ideal battery and electronics materials, respectively.

© 2022 Published by Elsevier B.V. on behalf of Chinese Chemical Society and Institute of Materia Medica, Chinese Academy of Medical Sciences.

Since the discovery of graphene, two-dimensional (2D) layered materials have exhibited excellent electrical, optical and mechanical properties due to their unique electrical structure and quantum confinement effect, and they are widely applied in optoelectronic semiconductor devices, flexible electronic devices, energy storage, and photoelectrocatalysis [1–5]. In particular, single-layer 2D materials with atomic thickness, namely monolayers, are attractive for applications in next-generation nanoelectronic devices which may cause low energy consumption [2,3,6–13]. Therefore, searching novel, efficient and feasible monolayers manifests important theoretical and practical values.

Bismuth based 2D materials have gradually become a hot research due to a larger number of advantages, such as, very kinds of species, abilities to adsorb visible light for most of materials, narrow band gap energy, low cost and non-toxicity [12–20]. Some elemental monolayers of bismuth, such as  $\beta$ -phase bismuthene with buckled hexagonal honeycomb structure and direct band gap of

0.32 eV and  $\alpha$ -phase bismuthene with puckered black-phosphorus style structure, have also theoretically found and experimentally synthesized [15–17]. For the binary compounds of group-VA including the bismuth element, BiN [21], BiP [22], BiAs [23], BiSi [24] semiconducting monolayers are all found or experimentally synthesized. On the other hand, for the binary compounds between bismuth and group-IVA family elements, two hexagonal SiBi monolayers with direct/indirect band gap of 0.674/0.4 eV [25,26], a tetragonal SiBi monolayer with indirect band gap of 0.554 eV [27], a metallic  $\alpha$ -phase CBi monolayer [28,29] and a Bi<sub>2</sub>C<sub>3</sub> monolayer with 12-atoms honeycomb lattices and direct bandgap of 1.23 eV [30] also have been predicted and studied respectively.

It is useful for developing new monolayers as CO<sub>2</sub> capture or storage materials in the practical applications. Recently, Kumar *et al.* studied the adsorption of NH<sub>3</sub>, NO and NO<sub>2</sub> gas molecules on the surface of a Bi<sub>2</sub>C<sub>3</sub> monolayer which can be used as a promising and sensitive sensor for above gasses [31]. On that account, by performing structure searching between carbon and bismuth elements using

Crystal structure analysis by particle swarm optimization (CALYPSO) package [32,33], we acquired two new stable monolayers, namely BiC and Bi<sub>2</sub>C monolayers, and discussed the applications

\* Corresponding authors.

E-mail addresses: [hec22019@xatu.edu.cn](mailto:hec22019@xatu.edu.cn) (C. He), [fxhuse@huse.edu.cn](mailto:fxhuse@huse.edu.cn) (X. Fu), [ful263@xatu.edu.cn](mailto:ful263@xatu.edu.cn) (L. Fu).

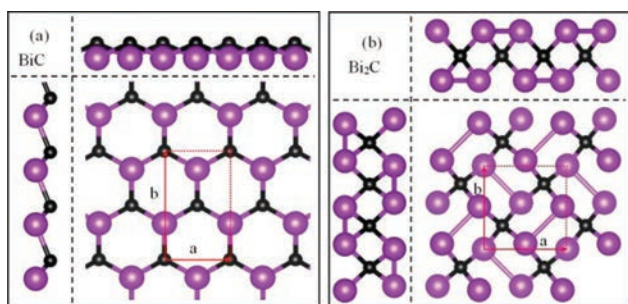


**Fig. 1.** Top and side views of (a) BiC and (b) Bi<sub>2</sub>C monolayer. Black and purple balls represent carbon and bismuth atoms, and their unit cells are shown in the top views.

of these monolayers in optoelectronics devices and electrocatalysis on CO<sub>2</sub> gas capture.

We used the Vienna *Ab-initio* simulation package (VASP) package and NANODCAL software with the generalized-gradient approximation (GGA)-Perdew-Burke-Ernzerh (PBE) functional to calculate the electronic, mechanical, optical properties, and to perform structure optimization in the predicting course using the CALYPSO package [34]. We set the energy cutoff as 600 eV and Monkhorst-Pack scheme as sample Brillouin zone with 0.02 Å<sup>-1</sup> spacing. The convergent energy per atom was set up to 1.0 × 10<sup>-6</sup> eV, and force of atom as no more than 0.001 eV/Å. On account of the large atomic number of bismuth element, spin-orbit coupling (SOC) should be considered when calculating the electronic properties of monolayers, and the HSE06 functional was also adopted to get more exact band gap [18,28,35]. Additionally, using the VASP package we implemented the first-principle molecular dynamics (MD) simulations in the NVT with a supercell of 3 × 3 × 1 or 3 × 4 × 1 at different temperatures from 100 K to 1400 K and at the 300 K equilibrium state, respectively. Finally, we employed the PHONOPY package to acquire the phonon spectrum with a supercell size as 4 × 4 × 1 [36].

Prediction was executed using the CALYPSO 6.0 package based on the method of global particle swarm optimization [32,33]. In the *input.dat* file, we opened the option of predicting 2D materials as 2D = T and set the parameters *Area* = 22, *MultiLayer* = 1, *DeltaZ* = 0.3 and *VacuumGap* = 14 Å to search Bi<sub>m</sub>C<sub>n</sub> monolayers. For a composition case, the numbers of generation and population size were 40 and 40 to acquire 1600 structures. The essential parameters in three *INCAR\_i* (*i* = 1, 2, 3) files were set as *NSW* = 60, 150, 300, *EDIFF* = 1e<sup>-2</sup>, 1e<sup>-3</sup>, 1e<sup>-5</sup> and *PSTRESS* = 0.001, respectively.

In the course of calculating CO<sub>2</sub> capture, Dmol<sup>3</sup> program package [37] was used in the whole structure optimization with the basis set as double numeric with polarization (DNP) [38]. The basis-set cutoff was set to 4.8 Å, and the K-point grid for Brillouin zones was 3 × 3 × 1 during geometry optimization. The Tkatchenko-Scheffler (TS) method of DFT-D correction [39] was used, and the vacuum layer was 20 Å [40]. All electrons in the system use core treatment in the entire structural optimization process and the charge distribution was determined by Hirshfeld analysis [41]. Additionally, a gas adsorption simulation was performed on a 2 × 3 × 1 supercell for the BiC structure, and a 2 × 2 × 1 supercell used for the Bi<sub>2</sub>C structure. In the course of calculating density of states (DOS), charge density difference and Crystal Orbital Hamiltonian Population (COHP) [42] properties, the K-point was set as 6 × 6 × 1.

Geometry structures of the BiC and Bi<sub>2</sub>C monolayers are shown in Fig. 1, and correspondingly their lattice parameters, bond lengths and cohesive energies are also presented in Table S1 (Supporting information). The space group of two monolayers are *P1*,

and unit cells of the BiC and Bi<sub>2</sub>C monolayers are taken as Bi<sub>2</sub>C<sub>2</sub> and Bi<sub>4</sub>C<sub>2</sub>. From Fig. 1a, the BiC monolayer has honeycomb hexagonal and buckled structures, and its structure in which C and Bi atoms are sp<sup>2</sup> hybridization, is extremely similar to that of β-phase bismuthene [12,18]. From Fig. 1b, the Bi<sub>2</sub>C monolayer, which looks like the structure of a buckled α-Bi monolayer [43], is composed of 5-membered rings including C-Bi single and Bi-Bi double bonds. In the structure, each C and Bi atoms form four bonds and three bonds respectively, all exhibiting sp<sup>3</sup> hybridization.

In Table S1, lengths of C-Bi bonds are 2.316 Å for the BiC monolayer, 2.317 Å and 2.319 Å for the Bi<sub>2</sub>C monolayer respectively, and there do not show relatively large differences to the lengths of Bi<sub>2</sub>C<sub>3</sub> monolayer (2.31 Å) and CBi monolayer (2.38 Å) [27,28]. Lengths of Bi-Bi bonds are 3.153 Å for the Bi<sub>2</sub>C monolayer, which are the same as that of 3.13 Å in the bismuthene or much smaller than that of 4.92 Å in the SiBi monolayer [18,44]. The bond lengths in two Bi-C monolayers are normal indicating they should be stable 2D materials.

Furthermore, we calculated their cohesive energy  $E_{\text{coh}}$  from the following formula:

$$E_{\text{coh}} = \frac{E_{\text{BimCn}} - mE_{\text{Bi}} - nE_{\text{C}}}{m + n} \quad (1)$$

where  $E_{\text{BimCn}}$ ,  $E_{\text{Bi}}$  and  $E_{\text{C}}$  are the energy of monolayer, one free Bi and one free C atom, respectively. As shown in Table S1,  $E_{\text{coh}}$  for the BiC and Bi<sub>2</sub>C monolayers are 4.304 and 4.29 eV/atom respectively, which are slightly smaller than that of 4.66 eV/atom for the Bi<sub>2</sub>C<sub>3</sub> monolayer [30], larger than that of 4.13 eV/atom for the CBi monolayer [28], 3.227 eV/atom for the SiBi monolayer [24], 2.896 eV/atom for the GeBi monolayer [27] and 2.697 eV/atom for the SnBi monolayer [27] respectively, further implying the stability of two Bi-C monolayers.

In order to show formation of bonds and charge transfer of two Bi-C monolayers, we calculated electron localization functions (ELFs) shown in Fig. S1 (Supporting information), and performed bader analysis presented in Table S2 (Supporting information) [45]. From Figs. S1a and b, two Bi-C monolayers exhibit electron collections between C and Bi, C and C, Bi and Bi atoms, indicating the formation of C-Bi, C-C, Bi-Bi bonds. In addition from the top and side views, there exist a mass of electrons around the Bi atoms, which leads to their metallic or semiconducting features. From Table S2, one can find that in the BiC monolayer about -0.802 charges and in the Bi<sub>2</sub>C monolayer -0.516 and -0.503 charges transfer from the Bi to the C atoms respectively, manifesting the formation of C-Bi bonds in two Bi-C monolayers.

Firstly, to study dynamic stability of two Bi-C monolayers, we calculated their phonon dispersion displayed in Figs. S2a and b (Supporting information). One can see that for the BiC and Bi<sub>2</sub>C monolayers no negative phonon frequencies exist which manifests two Bi-C monolayers are kinetically steady. Moreover, the slopes of acoustic branches for the BiC monolayer are identical along different orientations, such as G-M, G-K, showing it is isotropic related to the in-plane stiffness, and for the Bi<sub>2</sub>C monolayer its different slopes of acoustic branches indicate anisotropic property accordingly.

Secondly, we examined mechanical stability of two Bi-C monolayers by calculating their elastic constants ( $C_{ij}$ ). A mechanically stable 2D material should be conform to the Born criteria:  $C_{11} > 0$ ,  $C_{11}C_{22} > (C_{12})^2$ ,  $C_{66} > 0$  [46]. By fitting the energy curves relevant to in-plane stresses,  $C_{ij}$  were inferred as  $C_{11} = 54.75$  N/m,  $C_{22} = 54.52$  N/m,  $C_{12} = C_{21} = 16.38$  N/m,  $C_{66} = 4.814$  N/m for the BiC monolayer, and  $C_{11} = 13.21$  N/m,  $C_{22} = 33.56$  N/m,  $C_{12} = C_{21} = 5.06$  N/m,  $C_{66} = 0.95$  N/m for the Bi<sub>2</sub>C monolayer, respectively. These elastic constants are in accord with the Born criteria indicating their mechanical stability. Based on above elastic constants, in-plane Young's modules  $Y_x$  and  $Y_y$  can be deduced as

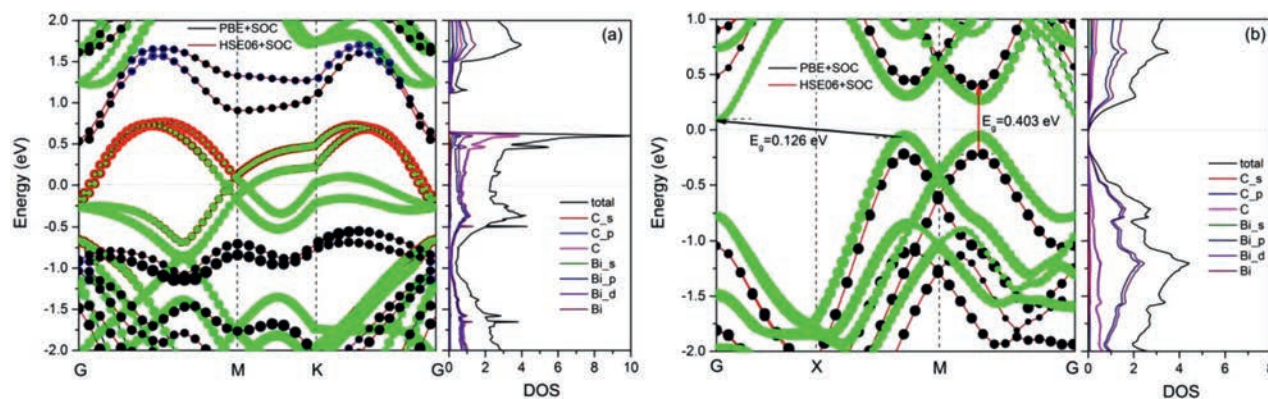


**Fig. 2.** Band structures and DOS of (a) BiC and (b) Bi<sub>2</sub>C monolayer with the GGA-PBE/HSE06 functional and the SOC effect. Green and red/black and blue rounds represent the weight of Bi and C atoms for the GGA-PBE/HSE06 functional, respectively.

49.83 and 49.62 N/m for the BiC monolayer, 12.44 and 31.62 N/m for the Bi<sub>2</sub>C monolayer, respectively. These values are smaller than those of MoS<sub>2</sub> monolayer (< 128 N/m), silicene (61 N/m) while the same as those of BiN monolayer [19,47], indicating two monolayers are relatively soft.

Finally, we performed first-principles MD simulations with a relatively large supercell  $4 \times 3 \times 1$  for the BiC monolayer,  $3 \times 3 \times 1$  for the Bi<sub>2</sub>C monolayer, respectively. After executing 10 ps simulations from 100 K to 1400 K, the structures of two monolayers maintain very well. We also executed 50 ps equilibrium simulations for two monolayers at the temperature 300 K which are shown in Fig. S3 (Supporting information). From Figs. S3a and b, the energy is oscillating near the equilibrium state and the structures of two monolayers are preserved well, displaying the thermal stability of two Bi-C monolayers which are anticipated to be experimentally practicable.

We calculated band structures and DOS of two Bi-C monolayers using the GGA-PBE and HSE06 functional, and the SOC effect was also considered to obtain more accurate band gap. Figs. S4a and b (Supporting information) show their band structures with/without SOC using the GGA-PBE functional and correspondingly high points are presented. When the SOC effect included, energy bands of two Bi-C monolayers all appear Rashba-type splits from the top of valence band. Additionally, this splitting will affect the positions of conduction band maximum (CBM) and valence band maximum (VBM) of two Bi-C monolayers and certainly deduce the changes of band gap [18,48]. Rashba coupling is one type of intrinsic SOC effects for possible control of spin states without a magnetic field, and can lead to spin degeneracy owing to structural inversion asymmetry [18].

Furthermore, in order to obtain precise band gap close to experimental possibilities, we also calculated band structures and DOS of two Bi-C monolayers including the SOC effect, which are displayed in Fig. 2. The BiC monolayer is metallic under the GGA-PBE (HSE06) functional. Its DOS strengths smaller than 0.5 eV mainly come from C atoms, and DOS strengths larger than 0.5 eV mainly come from Bi atoms. Moreover its DOS strengths for the p-orbital of all atoms are bigger than those of the s- and d-orbitals. The Bi<sub>2</sub>C monolayer is an indirect (direct) semiconductor with the band gap as 0.126 (0.403) eV under the GGA-PBE (HSE06) functional. Moreover, the DOS of Bi<sub>2</sub>C monolayer mainly comes from p-orbital of Bi atoms, and DOS strengths of Bi atoms are larger than that of C atoms. These results on the DOS verify that the carriers in two Bi-C monolayers mainly originate from Bi atoms or Bi p orbital once again. Liking the bismuthenes [18,49], the Bi<sub>2</sub>C monolayer is a narrow direct semiconductor, which makes it as an ideal 2D material in the applications of optoelectronics and photocatalysis. On the

other hand, in view of metallic speciality and honeycomb hexagonal structures liking graphene of the BiC monolayer, it can be as a potentially ideal battery or electrocatalysis material.

Base on band structures, we further calculated carrier mobilities of the Bi<sub>2</sub>C monolayer in consideration of its semiconducting, as shown in Table S3 (Supporting information) under the GGA-PBE functional. From the table, only the effective mass affects their carrier mobilities, then the mobilities were calculated as  $\mu_x = 194.67$ ,  $\mu_y = 139.05$  cm<sup>2</sup> V<sup>-1</sup> s<sup>-1</sup> for the electrons, and  $\mu_x = 69.22$ ,  $\mu_y = 6.38$  cm<sup>2</sup> V<sup>-1</sup> s<sup>-1</sup> for the holes respectively. The electron mobility along x direction is similar to the values of MoS<sub>2</sub> (200 cm<sup>2</sup> V<sup>-1</sup> s<sup>-1</sup>) and Bi<sub>2</sub>C<sub>3</sub> monolayer (186 cm<sup>2</sup> V<sup>-1</sup> s<sup>-1</sup>) [28,50], displaying the Bi<sub>2</sub>C monolayer is still a good semiconducting 2D material potentially applied in nanoelectronics.

It is great need to develop an efficient CO<sub>2</sub> removal system, and two-dimensional materials are considered as efficient CO<sub>2</sub> adsorbents [51,52]. To describe the interaction between CO<sub>2</sub> and BiC/Bi<sub>2</sub>C monolayer, we defined the adsorption energy  $E_{ad}$  as:

$$E_{ad} = E_{all} - E_{sub} - E_{gas} \quad (2)$$

where  $E_{all}$ ,  $E_{sub}$  and  $E_{gas}$  represent total energy of adsorbed monolayer, pristine BiC/Bi<sub>2</sub>C monolayer and the CO<sub>2</sub> molecule, respectively. The charge density difference  $\Delta\rho$  for the complexes was calculated by following equation:

$$\Delta\rho = \rho_{all} - (\rho_{sub} + \rho_{gas}) \quad (3)$$

where  $\rho_{all}$ ,  $\rho_{sub}$  and  $\rho_{gas}$  are charge density of adsorption system, BiC/Bi<sub>2</sub>C monolayer and the CO<sub>2</sub> molecule, respectively.

The adsorption of a single CO<sub>2</sub> gas molecule on the BiC monolayer was computed. In order to explore the most stable adsorption structure, several traditional adsorption sites were selected on the six-membered ring of BiC monolayer, namely top position of Bi atom (T1 site), hollow position (H1 site) and bridge position (Br site) of Bi-C bond, top position (C1 site) and back position (C2 site) of C atom, as shown in Figs. 3a and d. After calculations, the corresponding adsorption energies of five adsorption sites (T1, H1, Br, C1, C2) are -0.41, -0.21, -0.44, -0.25, -0.57 eV, respectively. Smaller the negative  $E_{ad}$  is, accordingly stronger the interaction and the exothermic reaction, which proves that the adsorption is reasonable and easy to occur.

According to the above data, it is easy to see that the C2 site is the most stable position for the adsorbed CO<sub>2</sub> gas molecule on the BiC monolayer, and corresponding most favorable adsorption structure was shown in Figs. 3b and e. From the figures it can be concluded that compared with free state CO<sub>2</sub> molecule, after being adsorbed the molecular configuration has been significantly bent, in which the  $\angle O-C-O$  bond angle is reduced from 180° to 124.3°

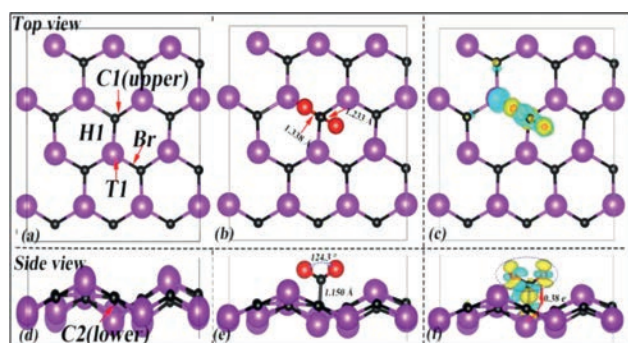


**Fig. 3.** (a, d) Top and side views of tested adsorption sites on the BiC monolayer. (b, e) The structure of BiC monolayer with the CO<sub>2</sub> adsorbed on the C2 site. (c, f) Corresponding difference charge density of BiC monolayer, and yellow/cyan area is the part where the charge density increases/decreases with the isosurface value as 0.008 e<sup>-</sup>/Bohr<sup>3</sup>.

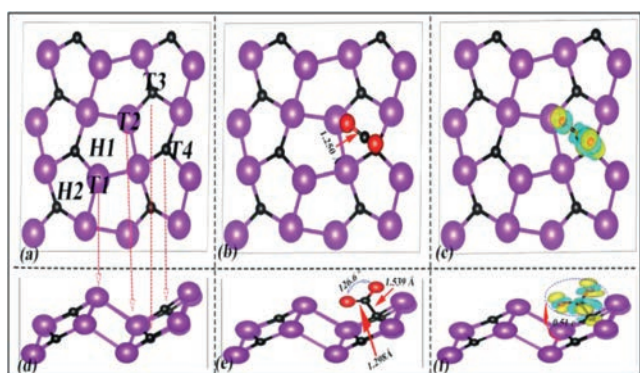


**Fig. 4.** (a, d) Top and side views of tested adsorption sites on the Bi<sub>2</sub>C monolayer. (b, e) The structure of Bi<sub>2</sub>C monolayer adsorbed CO<sub>2</sub> molecule at the T4 site. (c, f) Corresponding difference charge density of Bi<sub>2</sub>C monolayer.

and the C–O bond lengths are stretched from 1.177 Å to the maximum of 1.338 Å by 14%. The adsorption distance  $D_a$  between the monolayer and the substrate is 1.150 Å, which shows that the CO<sub>2</sub> gas has been violently activated on the BiC monolayer, and the BiC monolayer may have potential applications for CO<sub>2</sub> catalytic reduction.

When the  $E_{ad}$  is greater than  $-0.50$  eV, gas molecules can be effectively captured by the adsorbent [53]. Because the  $E_{ad}$  of CO<sub>2</sub> molecule at the C2 site is  $-0.57$  eV which corresponding to significant changes of the configuration for the CO<sub>2</sub> molecule, and by the Hirshfeld charge analysis it is easy to figure that the CO<sub>2</sub> molecule obtains  $0.38 e^-$  from the substrate during the adsorption process. Compared with the charge of C atom in the free state CO<sub>2</sub> molecule, the charge of C atom decreased from  $0.30 e^-$  to  $0.11 e^-$ , and the charge of O atoms increased from  $-0.15 e^-$  to  $-0.25 e^-$ , which is also consistent with the information reflected by charge density difference in Figs. 3c and f. In Figs. 3c and f, the electron density at the position of C atom in the CO<sub>2</sub> molecule decreases, while more electrons concentrate between the gas molecule and the monolayer, which indicates that C–O bond became weaken and a strong interaction between CO<sub>2</sub> molecules and BiC monolayer.

Using the same adsorption test method, for the Bi<sub>2</sub>C monolayer we chose the adsorption sites of CO<sub>2</sub> molecule as H1 and H2 (hollow sites), T1 (top site of raised Bi atoms), T2 (top site of sunken Bi atom), T3 (top site of C atoms in the lower layer), and T4 (top site of C atoms in the upper layer) respectively. Figs. 4a and d show six selected adsorption sites, and corresponding adsorption energy  $E_{ad}$  is 0.62, 0.67,  $-0.10$ , 1.22,  $-0.51$ ,  $-0.81$  eV. From Figs. 4b and e the configuration of CO<sub>2</sub> molecular at the T4 site has significantly changed due to strong adsorption interaction of the Bi<sub>2</sub>C mono-

layer, in which the  $\angle O-C-O$  bond angle is reduced from  $180^\circ$  to  $126.6^\circ$  and the C–O bond lengths are stretched from 1.177 Å to the maximum of 1.298 Å by 16%. The adsorption distance  $D_a$  between the CO<sub>2</sub> molecular and the Bi<sub>2</sub>C monolayer is 1.539 Å, which is larger than that of BiC monolayer. Figs. 4c and f show that the CO<sub>2</sub> molecule gets  $0.54 e^-$  from the Bi<sub>2</sub>C monolayer with the charge of C atoms changed from  $0.30 e^-$  to  $0.08 e^-$  and the charge of O atoms increased to  $-0.30 e^-$ . Corresponding charge density distribution diagram also indicates that there have distinct electrons flowing from C atoms to O atoms in the CO<sub>2</sub> molecule.

Similarly in Fig. S5 (Supporting information), the C atom at the T3 site can also effectively captures a CO<sub>2</sub> gas molecule with the  $E_{ad}$  as  $-0.51$  eV. From Figs. S5b and e, the bond length and bond angle of CO<sub>2</sub> molecule also changed obviously under the action of C atom at the T3 site, in which  $\angle O-C-O$  bond angle is reduced from  $180^\circ$  to  $126.2^\circ$ , and the C–O bond lengths are stretched from 1.177 Å to the maximum of 1.280 Å by 15%. The results on the Hirshfeld charge analysis show that the CO<sub>2</sub> molecule obtains  $0.49 e^-$  charge from the Bi<sub>2</sub>C monolayer after adsorption, and the map on the electron density difference presents that the electron population in the CO<sub>2</sub> molecule is transferred from the C atom to two O atoms. According to the analysis of above consequences on the degree of activation to C–O bonds ( $16\% > 15\% > 10\%$ ), the rank of activation ability for three sites on the adsorption of CO<sub>2</sub> molecule is T4 (Bi<sub>2</sub>C) > T3 (Bi<sub>2</sub>C) > C2 (BiC).

It is well known that the activation of C–O bonds in the CO<sub>2</sub> catalysis process is a prerequisite for the reduction process [54]. In order to figure out the activation of C–O bonds in the CO<sub>2</sub> molecule, we use molecular orbital theory [55] to study why the CO<sub>2</sub> molecule can be activated on the BiC/Bi<sub>2</sub>C monolayer. Fig. S5d shows the molecular orbital of free CO<sub>2</sub> molecule, and the smaller the difference in the energy level of atomic orbital, the stronger the performance ability of composed molecular orbital. Combining the DOS and COHP in Fig. S6a (Supporting information), it can be known that the bonding orbitals  $1\sigma 2\sigma 1\pi 2\pi$  of C–O bonds in free CO<sub>2</sub> molecule are mixed contributed by C  $p_z$ , O  $p_z$ , O  $p_y$ , C  $p_y$ , C  $p_x$ , O  $p_x$  atomic orbitals, and the non-bonded states are mainly composed of O  $p_x$ , O  $p_y$  and C  $p_z$  whose energy levels are around Fermi level. The anti-bond state is mainly contributed by the combination of C  $p_x$ , C  $p_y$ , C  $p_z$  and O  $p_y$ , respectively. From Fig. S6b (Supporting information) it can be seen that due to the activation at the T3 site of Bi<sub>2</sub>C monolayer, the bonded and non-bonded states of CO<sub>2</sub> molecule have undergone significant changes. Moreover, the corresponding bonded state has shifted to a deeper energy level from  $-4.2$  eV to  $-6.3$  eV, and the non-bonded state has shifted from  $-4.5$  eV to 0 eV which corresponding to a wider range. The bonding state of C–O bonds at this time is mainly composed of the contributions of O  $p_x$ , O  $p_z$  and C  $p_y$  atomic orbitals. The contribution of O  $p_y$  atomic orbital to the non-bonded state and the area of anti-bonding state increase, indicating that due to more anti-bonding orbitals the C–O bonds are weakened after the linearly mixing of atomic orbitals again.

Similarly, by comparing Fig. S6c (Supporting information) at the T4 site of Bi<sub>2</sub>C monolayer with Fig. S6b, one can conclude that the bonded states are mostly composed of O p and C p atomic orbitals which localized around  $-6.2$  eV, and the range of non-bonded states from  $-4.1$  eV to 0 eV mainly composed of O p orbitals which is not as wide as that of the T3 site. Compared to the area of anti-bonding state shown in Fig. S6a, the area of anti-bonding state in Fig. S6c is increased, indicating that the C–O bonds are also weakened atomic orbitals. As for the C2 site of BiC monolayer to activate the CO<sub>2</sub> molecule in Fig. S6d (Supporting information), we find that the non-bonded orbitals are mainly composed of C  $p_x$ , C  $p_y$  and C  $p_z$  atomic orbitals, and the range of bonded states (mainly concentrated at  $-5.5$  to  $-6.1$  eV) are mainly composed of C  $p_x$ , C  $p_y$  and C  $p_z$  contribution composition.

The Intergral Crystal Orbital Hamiltonian Population (ICOHP) of C–O bonds at the T3, T4 and C2 sites are  $-12.52$ ,  $-12.10$  and  $-11.14$  respectively, which are reduced by 31.9%, 34.2% and 39.4% compared with free CO<sub>2</sub> molecule case, and further proved the activation of C–O bonds. In summary, the reason why BiC/Bi<sub>2</sub>C monolayer is more capable of activating the C–O bonds in the CO<sub>2</sub> molecular is that the C atom (bonded with Bi atom) regulating the electronic structure of CO<sub>2</sub> molecular, which resulting the changes of CO<sub>2</sub> molecular orbital distribution. The BiC and Bi<sub>2</sub>C monolayers can be used as promising adsorbents to capture CO<sub>2</sub> gas aiming to mitigate the greenhouse effect.

In conclusion, we used the CALYPSO methodology obtaining two bismuth carbide monolayers. By including the SOC effect, the BiC monolayer is a metal and the Bi<sub>2</sub>C monolayer is a direct semiconductor with the band gap as 0.403 eV. For the adsorption of CO<sub>2</sub> molecules on two monolayers, the BiC monolayer has one stable site C2, and the Bi<sub>2</sub>C monolayer has two stable sites T3 and T4. Based on the molecular orbital theory and ICOHP analysis, the rank of activation ability for three sites on the adsorption of CO<sub>2</sub> molecules is T4 > T3 > C2. Therefore, one can concluded that the BiC and Bi<sub>2</sub>C monolayers are promising adsorbents to capture CO<sub>2</sub> gas being expected to mitigate the greenhouse effect. The Bi<sub>2</sub>C monolayer also has a wide scope of applications in the optoelectronics and photocatalysis for its narrow direct band gap and good carrier mobility. As to the Bi<sub>2</sub>C monolayer, it is metallic and may be applied in the energy storage battery.

#### Declaration of competing interest

The authors declare that they have no known competing financial interests or personal relationships that could have appeared to influence the work reported in this paper.

#### Acknowledgments

We thank hongzhiwei cloud platform to provide computer time. This study was funded by the Natural Science Foundation of China (Nos. 21603109, 11304128), the Henan Joint Fund of the National Natural Science Foundation of China (No. U1404216), the Science and Technology Program of Henan Department of Science and Technology, China (No. 182102310609), and the Construct Program of Applied Characteristic Discipline in Hunan University of Science and Engineering (Mathematics, Education and Electronic Science and Technology).

#### Supplementary materials

Supplementary material associated with this article can be found, in the online version, at doi:10.1016/j.ccl.2021.12.041.

#### References

- [1] D. Akinwande, C. Huyghebaert, C.H. Wang, et al., *Nature* 573 (2019) 507–518.

- [2] X.D. Zhang, Y. Xie, *Chem. Soc. Rev.* 42 (2013) 8187.  
[3] G.R. Xu, H. Li, A.S.R. Bati, et al., *J. Mater. Chem. A* 8 (2020) 15875–15883.  
[4] D.W. Zhou, C.P. Li, F.R. Yin, et al., *Chin. Chem. Lett.* 31 (2020) 2325–2329.  
[5] C.Y. Pu, J.H. Yu, L. Fu, et al., *Chin. Chem. Lett.* 32 (2021) 1081–1085.  
[6] L. Fu, L.B. Yan, L. Lin, et al., *J. Alloys. Comp.* 875 (2021) 159907.  
[7] C.Z. He, J. Wang, L. Fu, C.X. Zhao, J.R. Huo, *Chin. Chem. Lett.* 33 (2022) 1051–1057.  
[8] C.Z. He, H.T. Wang, L. Fu, et al., *Chin. Chem. Lett.* 33 (2022) 990–994.  
[9] Y.C. Wang, Y. Liu, W. Liu, et al., *Energy Environ. Sci.* 13 (2020) 4609–4624.  
[10] H.Y. Jing, P. Zhu, X.B. Zheng, et al., *Adv. Powder Mater.* (2021), doi:10.1016/j.apmate.2021.10.004.  
[11] G.L. Liu, J.H. Zhou, W.N. Zhao, Z.M. Ao, T.C. An, *Chin. Chem. Lett.* 31 (2020) 1966–1969.  
[12] X. Fu, H.Y. Yang, L. Fu, et al., *Chin. Chem. Lett.* 32 (2021) 1089–1094.  
[13] W.L. Li, Q.G. Jiang, D.D. Li, Z.M. Ao, T.C. An, *Chin. Chem. Lett.* 32 (2021) 2803–2806.  
[14] S.L. Zhang, S.Y. Guo, Z.F. Chen, et al., *Chem. Soc. Rev.* 47 (2018) 982–1021.  
[15] S. Singh, Z. Zanolli, M. Amsler, et al., *J. Phys. Chem. Lett.* 10 (2019) 7324–7332.  
[16] R.J. Gui, H. Jin, Y.J. Sun, X.W. Jiang, Z.J. Sun, *J. Mater. Chem. A* 7 (2019) 25712.  
[17] J. Zhang, S.A. Ye, Y. Sun, et al., *Nanoscale* 12 (2020) 20945–20951.  
[18] X.H. Liu, S.L. Zhang, S.Y. Guo, et al., *Chem. Soc. Rev.* 49 (2020) 263–285.  
[19] L. Cheng, H.J. Liu, X.J. Tan, et al., *J. Phys. Chem. C* 118 (2) (2014) 904–910.  
[20] K.H. Jin, E. Oh, R. Stania, F. Liu, H.W. Yeom, *Nano Lett.* 21 (2021) 9468–9475.  
[21] C.Z. He, R. Wang, D. Xiang, et al., *Appl. Surf. Sci.* 509 (2020) 145392.  
[22] H. Zhang, M.Y. Chen, *J. Mater. Chem. C* 6 (2018) 11694.  
[23] T. Teshome, A. Datta, *J. Phys. Chem. C* 122 (2018) 15047–15054.  
[24] Y.C. Wang, L. Xu, L.S. Zhan, et al., *Nano Energy* 22 (2022) 106780.  
[25] R.N. Somaiya, Y. Sonvane, S.K. Gupta, *Phys. Chem. Chem. Phys.* 22 (2020) 3990–3998.  
[26] A. Bafekry, F. Shojaei, M.M. Obeid, et al., *RSC Adv.* 10 (2020) 31894.  
[27] C.Y. Xu, M.F. Zhu, J.M. Zhang, W.Q. Wang, Y. Yan, *Comput. Mater. Sci.* 150 (2018) 314–320.  
[28] R. Wang, C.Z. He, W.X. Chen, C.X. Zhao, J.R. Huo, *Chin. Chem. Lett.* 32 (2021) 3821–3824.  
[29] B. Özdamar, G. Özbal, M.N. Çınar, et al., *Phys. Rev. B* 98 (2018) 045431.  
[30] P.F. Liu, T. Bo, Z.F. Liu, et al., *J. Mater. Chem. C* 6 (2018) 12689.  
[31] V. Kumara, K. Rajputa, D.R. Roy, *Appl. Surf. Sci.* 534 (2020) 147609.  
[32] Y.C. Wang, M.S. Miao, J. Lv, et al., *J. Chem. Phys.* 137 (2012) 224108.  
[33] X.Y. Luo, J.H. Yang, H.Y. Liu, et al., *J. Am. Chem. Soc.* 133 (2011) 16285.  
[34] G. Kresse, D. Joubert, *Phys. Rev. B* 59 (1999) 1758.  
[35] J. Paier, M. Marsman, K. Hummer, et al., *J. Chem. Phys.* 124 (2006) 154709.  
[36] A. Togo, I. Tanaka, *Scrip. Mater.* 108 (2015) 1–5.  
[37] B. Delley, *J. Chem. Phys.* 113 (2000) 7756–7764.  
[38] W. Xi, K. Wang, Y. Shen, et al., *Nat. Commun.* 11 (2020) 1919.  
[39] R.M.A. Khalil, *Chin. J. Phys.* 54 (2016) 890–894.  
[40] C. He, R. Wang, D. Xiang, et al., *Appl. Surf. Sci.* 507 (2020) 145076.  
[41] A.V. Marenich, S.V. Jerome, C.J. Cramer, D.G. Truhlar, *J. Chem. Theor. Comput.* 8 (2012) 527–541.  
[42] V.L. Deringer, A.L. Tchougreff, R. Dronskowski, *J. Phys. Chem. A* 115 (2011) 5461–5466.  
[43] Y.G. Guo, H.Q. Zhu, Q. Wang, *J. Phys. Chem. C* 124 (2020) 5506–5513.  
[44] M.Y. Liu, Y. Huang, Q.Y. Chen, et al., *RSC Adv.* 7 (2017) 39546.  
[45] P.F. Liu, L.J. Zhou, T. Frauenheimb, L.M. Wu, *Phys. Chem. Chem. Phys.* 18 (2016) 30379–30384.  
[46] S.J. Liu, B. Liu, X.H. Shi, et al., *Sci. Rep.* 7 (2017) 2404.  
[47] D. Fan, S.H. Lu, Y.D. Guo, X.J. Hu, *J. Mater. Chem. C* 6 (2018) 1651.  
[48] E. Akturk, O.U. Akturk, S. Ciraci, *Phys. Rev. B* 94 (2016) 014115.  
[49] C. Shen, T.L. Cheng, C.Y. Liu, et al., *J. Mater. Chem. A* 8 (2020) 453.  
[50] B. Rajbanshi, P. Sarkar, *J. Phys. Chem. Lett.* 8 (2017) 747–754.  
[51] H.Y. Yang, C.Z. He, L. Fu, J.R. Huo, C.X. Zhao, *Chin. Chem. Lett.* 32 (2021) 3202–3206.  
[52] L. Fu, R. Wang, C.X. Zhao, et al., *Chem. Eng. J.* 414 (2021) 128857.  
[53] X. Ma, Y. Shen, S. Yao, et al., *J. Mater. Chem. A* 8 (2020) 3344–3350.  
[54] J.H. Yu, C.Z. He, C.Y. Pu, et al., *Chin. Chem. Lett.* 32 (2021) 3149–3154.  
[55] Q. Li, Y.C. Wang, J. Zeng, et al., *Rare Metal.* 40 (2021) 3442–3453.